Chemical Science

ROYAL SOCIETY OF CHEMISTRY

EDGE ARTICLE

View Article Online
View Journal | View Issue



Cite this: *Chem. Sci.*, 2025, **16**, 4876

All publication charges for this article have been paid for by the Royal Society of Chemistry

Received 22nd November 2024
Accepted 31st January 2025

DOI: 10.1039/d4sc07901a

rsc.li/chemical-science



# Inverse opal anatase/rutile $TiO_2$ multi-heterojunctions enable efficient photoelectrochemical water splitting†

Bo-Hao Xiao,[ab] Chen Huo,[a] Jin-Yu Chen,[a] Ying-Guan Xiao,[ac] Shun-Sheng Cao *[a] and Zhao-Qing Liu *[bd]

$TiO_2$ has garnered significant attention in the field of photoelectrochemical (PEC) water splitting due to its non-toxicity, cost-effectiveness, and exceptional photochemical stability. However, its practical efficiency in $H_2$ production is greatly hindered by inherent limitations such as low electron mobility, a short carrier diffusion length, and a wide optical band gap. Herein, we present a strategy of combining a crystal phase heterojunction and crystal facet heterojunction to enhance electron–hole separation efficiency in $TiO_2$. The crystal facet heterojunction of rutile $TiO_2$ extends the photogenerated electron lifetime by exploiting discontinuous band gaps and accelerates space charge separation. Moreover, the band alignment between rutile and anatase $TiO_2$ is favorable for electron transfer from rutile to anatase through a phase heterojunction. Consequently, the inverse opal anatase/rutile $TiO_2$ nanorod (IO-$TiO_2$/NRs-$TiO_2$) photoanode affords an excellent hydrogen production rate (682 μmol $h^{-1}$ $g^{-1}$), which is 1.6 times higher than that of an inverse opal anatase/rutile $TiO_2$ single heterojunction and 3 times higher than that of inverse opal anatase. This work provides valuable insights into the rational design of photoanodes with a 3D hierarchical structure.

## Introduction

Sunlight-driven photoelectrochemical (PEC) hydrogen generation represents a promising strategy for addressing the energy crisis and environmental pollution challenges.[1] However, the low conversion efficiency of solar energy to hydrogen and the slow light absorption, charge separation and reaction kinetics hinder the widespread application of PEC water splitting.[2,3] Therefore, exploring and designing photocatalysts to effectively promote photoinduced charge separation and transfer is a critical scientific issue that needs to be addressed urgently.[4]

Since the pioneering work of Fuji Shima and Honda, who first reported PEC water splitting using $TiO_2$ as a working electrode, extensive investigations have been conducted on $TiO_2$ for PEC or photocatalytic water splitting due to its non-toxicity, low cost, high photochemical stability, and resistance to photo corrosion.[5,6] However, the practical solar-to-hydrogen efficiency of $TiO_2$ is significantly limited by its low electron mobility (1 $cm^2$ $V^{-1}$ $s^{-1}$), short minority carrier diffusion length (10–100 nm), and wide optical band gap (3.2 eV for anatase).[7] Rutile $TiO_2$ theoretically possesses greater potential as a photoanode due to its higher thermostability, more efficient charge separation, and smaller bandgap compared to anatase $TiO_2$. However, rutile $TiO_2$ often exhibits lower PEC performance than anatase $TiO_2$ due to the increased recombination rate of electron–hole pairs.[8,9] Moreover, anatase $TiO_2$ is an indirect bandgap semiconductor, indicating that photoinduced electrons can be readily separated from holes, thereby enhancing the electron lifetime.[10]

Rational design of the material structure is a crucial strategy for suppressing charge recombination and enhancing light absorption.[11] Among these strategies, the construction of host–guest heterojunction electrodes using different dimensional nanostructures has been demonstrated to effectively facilitate charge transport and suppress electron–hole pair recombination, resulting in superior performance in PEC applications.[12,13] In such nanostructures, the host semiconductor with a large surface area and high chemical stability acts as a scaffold for the growth of guest conductive materials. This facilitates efficient collection of electrons generated within the guest materials, thereby reducing bulk charge recombination.[12,14] For instance, 3D hierarchical structures or arrays such as FTO/FTO-

[a]*Research School of Polymer Materials, School of Materials Science and Engineering, Jiangsu University, Zhenjiang 212013, China. E-mail: sscao@ujs.edu.cn*

[b]*School of Chemistry and Chemical Engineering, Guangzhou Key Laboratory for Clean Energy and Materials, Guangzhou University, Guangzhou 510006, P. R. China. E-mail: lzqgzu@gzhu.edu.cn*

[c]*School of Safety Management, Guangxi Vocational College of Safety Engineering, Nanning 530100, China*

[d]*School of Chemistry, South China Normal University, Guangzhou 510006, P. R. China*

† Electronic supplementary information (ESI) available: Experimental details, SEM images, EDS element mapping, AFM analysis, XPS spectra, UV-vis absorption spectra, LSV curves, and EIS. See DOI: https://doi.org/10.1039/d4sc07901a

nanocrystal/$TiO_2$,[14] IOs/CdS NRs/CdSe clusters,[12] $SnO_2$/$TiO_2$/$BiVO_4$ arrays,[13] and $TiO_2$/$WO_3$/$BiVO_4$ arrays,[15] have been reported to enhance the light harvesting and charge transport performance due to the synergistic effects of these component nanostructures. Although $TiO_2$ is very attractive due to its relatively negative flat band potential and good chemical stability, the intrinsically low mobility of $TiO_2$ still considerably limits the overall PEC performance of $TiO_2$-based heterojunction photoanodes.[13] Notably, tuning heterojunction nanostructures is also a promising strategy to suppress charge recombination in PEC water splitting, such as heterojunctions,[16] phase junctions,[17] facet junctions,[18] and Schottky junctions.[19]

Inspired by the concept of junction-structure design, we propose an effective strategy to enhance charge separation and transfer efficiency of $TiO_2$ by incorporating anatase/rutile heterojunctions with rutile facet heterojunctions. Specifically, inverse opal anatase (IO-$TiO_2$) is used as a skeleton for the growth of rutile $TiO_2$ nanorods (NRs), and then the rutile facet heterojunction is further formed by using NRs as a substrate (NRs-$TiO_2$). In this hierarchical photoanode (IO-$TiO_2$/NRs-$TiO_2$), highly oriented IO-$TiO_2$ plays the role of a conductive skeleton to collect electrons and its face-centered cubic periodic void structure can facilitate the infiltration of the electrolyte solution and promote light scattering. Secondly, the crystal phase heterojunction material shows higher PEC activity than each individual phase due to the disorder of the $TiO_2$ lattice at the phase junction. The facet junction in rutile $TiO_2$ can prolong the lifetime of photoinduced electrons by bandgap discontinuity, accelerating spatial charge separation. Consequently, the 3D IO-$TiO_2$/NRs-$TiO_2$ photoanode shows excellent hydrogen production efficiency for water splitting, which is 1.6 and 3.0 times higher than that of IO-$TiO_2$/NRs and IO-$TiO_2$, respectively. The 3D multi-level structure constructed in this work provides new insights into the rational design of host–guest heterojunction electrodes for highly efficient PEC reactions.

## Results and discussion

The impact of the crystal phase heterojunction and crystal plane heterojunction on the charge separation and transfer efficiency of the IO-$TiO_2$/NRs-$TiO_2$ photoanode was confirmed through DFT calculations. The results from band structure calculations demonstrate an optimal interlaced arrangement between different crystal faces of anatase and rutile, facilitating REDOX reactions and charge transfer (Fig. 1a).[20] The partial density of states (PDOS) of anatase and rutile $TiO_2$ reveals that the band gap value for anatase is measured to be 3.16 eV, whereas the band gap value for rutile is slightly reduced to 2.87 eV (Fig. 1b). Consequently, it can be anticipated that the construction of crystal phase heterojunctions will diminish the charge transfer energy of anatase, thereby facilitating electron transitions from the valence band to the conduction band and engendering new hole–electron pairs.[21] Moreover, the work function is a crucial parameter for investigating electron transfer in heterogeneous structures, which can be estimated by calculating the energy difference between the vacuum and the Fermi level of the materials.[22,23] As shown in Fig. 1c–f, the work functions of anatase (101), rutile (110), rutile (111), and rutile (101) surfaces are determined to be 7.95, 7.89, 7.57, and 7.26 eV, respectively. Upon coupling the anatase/rutile phase heterojunction with the rutile surface heterojunction, driven by a potential difference, electrons will initially transfer from rutile (111)/(101) to rutile (110) through the surface heterointerface and subsequently from rutile (110) to anatase (101) across the heterogeneous interface until they reach equilibrium at identical energy levels.[21] In summary, the superior electronic structure and band alignment at the multi-heterojunction interface can promote electron participation in the catalytic process, thereby enhancing the charge separation and transfer efficiency of $TiO_2$.

The entire preparation process of the IO-$TiO_2$/NRs-$TiO_2$ photoanode is illustrated in Fig. 2a. First, the treated FTO conducting glass is coated with polystyrene spheres (Fig. 2b and S1a†), followed by the formation of highly ordered IO-$TiO_2$ with a pore size of approximately 230 nm through self-assembly of a TBT precursor and subsequent calcination at 450 °C (Fig. 2c and S1b†). Subsequently, NRs (~110 nm in length) are grown on the surface of IO-$TiO_2$ *via* a hydrothermal reaction (Fig. 2d and S1c†). Finally, rutile $TiO_2$ nanosheets (with lengths ranging from 2–7 nm) are grown on the provided template by the hydrothermal method, resulting in the formation of a 3D multi-heterojunction photoanode denoted as IO-$TiO_2$/NRs-$TiO_2$ (Fig. 2e and S1d†). Varying amounts of both TBT ($TiO_2$ nanorod precursor) and $TiCl_3$ ($TiO_2$ nanosheet precursor) exert notable influences on the structure and morphology of NRs as well as on the coated rutile $TiO_2$ nanosheets (Fig. S2†). Among them, the IO-$TiO_2$/NRs-$TiO_2$ photoanode with TBT-0.15 mL and $TiCl_3$-0.25 mL exhibits optimal morphology and nanostructures, and was chosen as the target sample. Notably, TEM (Fig. 2f and S3†) and HRTEM images confirm the presence of a crystal phase and crystal plane heterojunction, including anatase/rutile heterostructures (Fig. 2g) and rutile (111)/(101) heterostructures, respectively (Fig. 2h).[10,24,25] The presence of anatase and rutile phases in the sample was confirmed by selective area electron diffraction (Fig. S4†). Furthermore, the elemental distribution exhibits suitable ratios of Ti, O, and C elements in IO-$TiO_2$/NRs-$TiO_2$ with a highly uniform distribution (Fig. 2i and S5†).

Scanning transmission electron microscope (STEM) images of NRs-$TiO_2$ within IO-$TiO_2$/NRs-$TiO_2$ also provide additional evidence for the uniform distribution of Ti, O, and C elements as well as the formation of crystal heterojunctions (Fig. S6†). The cross-section morphology of IO-$TiO_2$/NRs-$TiO_2$ further confirms its 3D hierarchical structure (Fig. S7†). Moreover, the structure of the IO-$TiO_2$/NRs-$TiO_2$ sample was further investigated using atomic force microscopy. The current peak indicated by the dotted line corresponds to the height change curve (Fig. S8†), and it can be observed that these current peaks are predominantly located near the junctions of crystal phases and crystal facet heterojunctions. Within the pure IO-$TiO_2$ range corresponding to the height change curve, all current values are consistently lower and tend to remain flat, thereby revealing successful preparation of a multi-heterojunction system that significantly enhances carrier mobility.

The crystal structures of FTO, IO-$TiO_2$, IO-$TiO_2$/NRs, and IO-$TiO_2$/NRs-$TiO_2$ were investigated using X-ray diffraction (XRD).

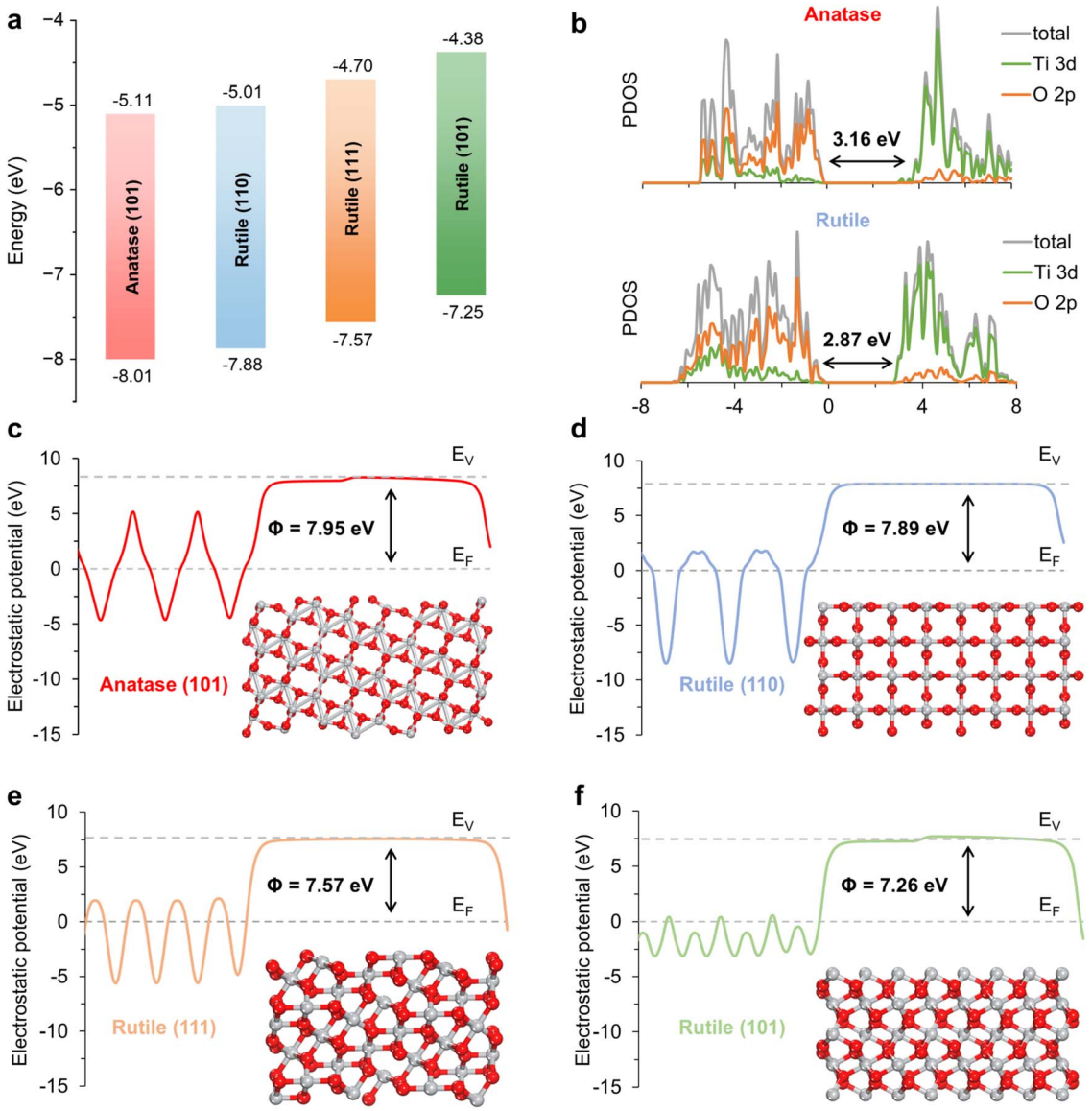


Fig. 1 (a) The band structures and migration of the charges and holes in anatase (101), rutile (110), rutile (111), and rutile (101) surfaces. (b) The partial density of states (PDOS) of anatase and rutile $TiO_2$ unit cells using the HSE 06 functional. The zero of the energy corresponds to the Fermi level. Electrostatic potential of (c) anatase (101), (d) rutile (110), (e) rutile (111), and (f) rutile (101) surfaces.

IO-$TiO_2$ exhibits distinct peaks at 25.3° and 48.0° as shown in Fig. 3a, corresponding to the characteristic peaks of anatase $TiO_2$. After growing NRs on the IO-$TiO_2$ surface, IO-$TiO_2$/NRs not only retains their anatase phase but also exhibits rutile characteristic diffraction peaks at 27.4° (110), 36.1° (101), and 62.7° (002). These results provide evidence for the successful formation of an anatase/rutile-phase junction between IO-$TiO_2$ and NRs. After further coating of $TiO_2$ nanosheets on NRs, an enhanced rutile phase is observed in IO-$TiO_2$/NRs-$TiO_2$. The composition of the prepared photoanode was further investigated using Raman spectroscopy. As displayed in Fig. 3b, while IO-$TiO_2$ only exhibits characteristic Raman peaks of anatase (402, 515, and 630 $cm^{-1}$), IO-$TiO_2$/NRs not only displays similar Raman peaks of anatase but also demonstrates weak Raman peaks corresponding to the rutile phase (232, 446, and 608 $cm^{-1}$), suggesting the construction of a phase heterojunction between IO-$TiO_2$ and NRs.[26] In contrast, IO-$TiO_2$/NRs-$TiO_2$ exhibits comparable Raman peaks for anatase and stronger peaks for the rutile phase, providing strong evidence for the formation of a facet heterojunction between NRs and the coated $TiO_2$ nanosheets.

The element composition and corresponding chemical environment of IO-$TiO_2$, IO-$TiO_2$/NRs, and IO-$TiO_2$/NRs-$TiO_2$ were determined by X-ray photoelectron spectroscopy (XPS) analysis. The presence of Ti, C, and O elements in IO-$TiO_2$/NRs-$TiO_2$ was confirmed by the XPS full spectrum (Fig. S9†). The Ti 2p peaks at 463.6–464.1 eV and 457.9–458.4 eV correspond to Ti $2p_{3/2}$ and Ti $2p_{1/2}$ respectively, which confirmed that Ti in the sample is in the +4 valence state (Fig. S10a†).[27] Two oxygen chemical states were observed: lattice oxygen with a binding

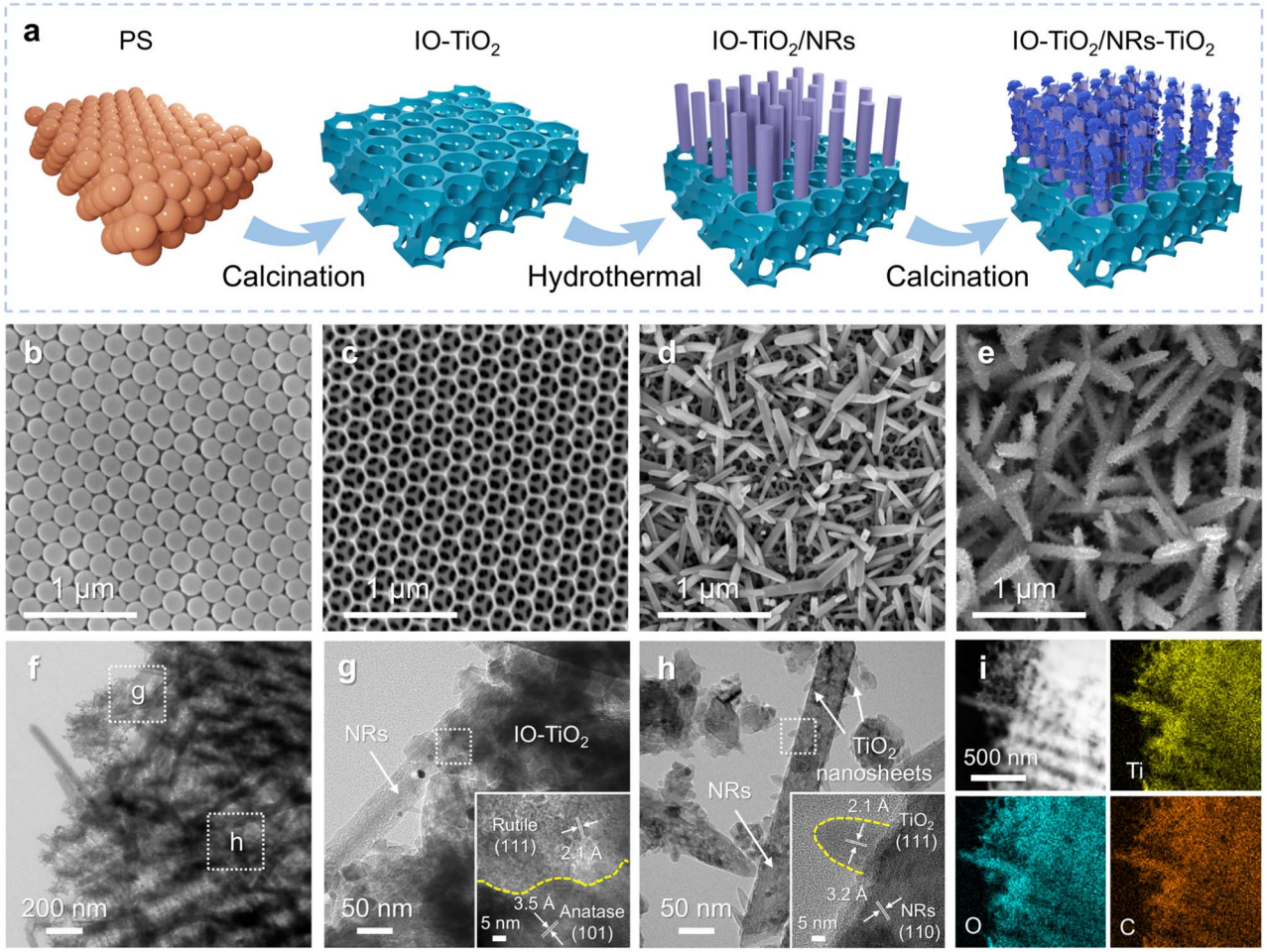


Fig. 2 (a) Schematic diagrams for IO-$TiO_2$/NRs-$TiO_2$. SEM images of (b) PS spheres, (c) IO-$TiO_2$, (d) IO-$TiO_2$/NRs, and (e) IO-$TiO_2$/NRs-$TiO_2$. TEM images of (f) IO-$TiO_2$/NRs-$TiO_2$, (g) the anatase/rutile heterojunction, and (h) the rutile crystal surface heterojunction. (i) EDS element mapping of IO-$TiO_2$/NRs-$TiO_2$.

energy range of 529.1–530.0 eV and hydroxyl oxygen with a BE range of 531.2–532.0 eV (Fig. S10b†).[28,29] Compared to IO-$TiO_2$, the Ti 2p peaks of IO-$TiO_2$/NRs exhibit a slight positive shift, indicating the successful integration of IO-$TiO_2$ and NRs. Upon coating with $TiO_2$ nanosheets, a further redshift in IO-$TiO_2$/NRs-$TiO_2$ suggests the formation of a facet heterojunction between NRs and the coated $TiO_2$ nanosheets. Meanwhile, the corresponding binding energy of O 1s shifts towards a more negative position, suggesting electron transfer to Ti atoms and hole transfer to O atoms after heterojunction formation.

The peak shifts of the three samples were investigated using *in situ* XPS measurement, revealing the impact of heterojunctions on the efficiency and transfer of photogenerated electrons.[30] Under light irradiation, the binding energies of Ti $2p_{3/2}$ and Ti $2p_{1/2}$ significantly shifted towards higher positions (Fig. 3c), while the O 1s peaks exhibited a shift towards lower values (Fig. 3d), indicating predominant transfer of separated electrons to O atoms and holes to Ti atoms.[31] Notably, IO-$TiO_2$ exhibits minimal shifts in the Ti $2p_{3/2}$ (~0.9 eV) and Ti-OH (~0.16 eV) peaks after light irradiation due to the high recombination rate of photoexcited charge pairs, while IO-$TiO_2$/NRs demonstrates significantly enhanced shifts in the Ti $2p_{3/2}$ (~1.1 eV) and Ti-OH (~0.4 eV) peaks owing to efficient photogenerated charge separation facilitated by the anatase/rutile heterojunction. IO-$TiO_2$/NRs-$TiO_2$ displays the most pronounced shifts in the Ti $2p_{3/2}$ (~1.5 eV) and Ti-OH (~1.0 eV) peaks, which may be mainly attributed to the formation of multiple heterojunctions. In addition, a notable reduction in the peak Ti-OH intensity of IO-$TiO_2$/NRs-$TiO_2$ under irradiation was observed. This decrease can be attributed to the excitation of electrons from the valence band to the conduction band upon exposure of IO-$TiO_2$/NRs-$TiO_2$ to visible light, leading to the formation of electron–hole pairs. These charge carriers facilitate the dissociation of $H_2O$ on the IO-$TiO_2$/NRs-$TiO_2$ surface. As the irradiation time increases, more Ti-OH groups engage in the photocatalytic reaction, consequently reducing the intensity of the corresponding peak. Based on these results, it can be concluded that multiple heterojunctions indeed promote more efficient charge separation and transfer.

We further investigated the light absorption of the samples. The results demonstrate that the IO-$TiO_2$/NRs-$TiO_2$ photocatalyst (TBT-0.15 mL and $TiCl_3$-0.25 mL) exhibits superior light adsorption compared to other samples, as evidenced by its morphology and nanostructures (Fig. S11†). Moreover, IO-$TiO_2$,

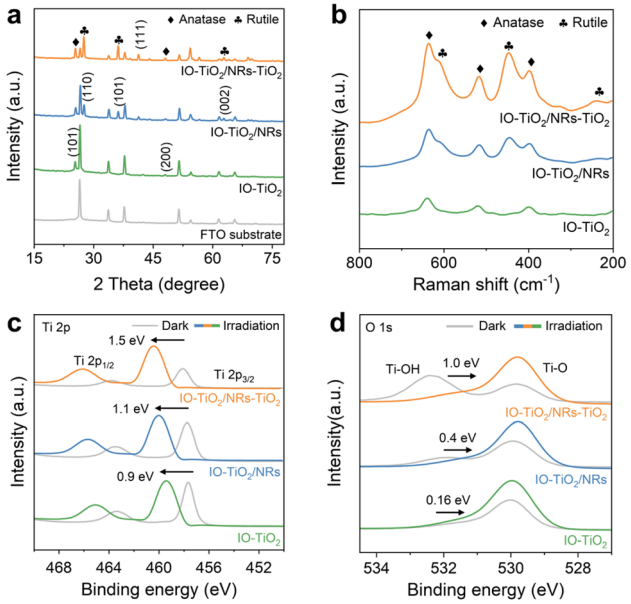


Fig. 3 (a) XRD patterns of FTO, IO-$TiO_2$, IO-$TiO_2$/NRs, and IO-$TiO_2$/NRs-$TiO_2$, (b) Raman spectra of IO-$TiO_2$, IO-$TiO_2$/NRs and IO-$TiO_2$/NRs-$TiO_2$. XPS spectra of IO-$TiO_2$, IO-$TiO_2$/NRs and IO-$TiO_2$/NRs-$TiO_2$ in dark and irradiated states: (c) Ti 2p and (d) O 1s.

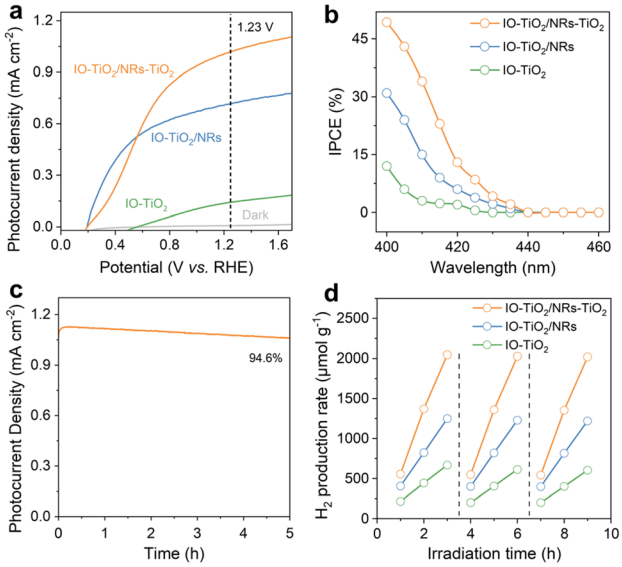


Fig. 4 (a) Linear sweep voltammetry (LSV) curves and (b) incident photon to current conversion efficiency (IPCE) of IO-$TiO_2$, IO-$TiO_2$/NRs and IO-$TiO_2$/NRs-$TiO_2$. (c) Long-term photocurrent–time curves of IO-$TiO_2$/NRs-$TiO_2$. (d) The cycling photocatalytic $H_2$-evolution test of IO-$TiO_2$, IO-$TiO_2$/NRs and IO-$TiO_2$/NRs-$TiO_2$.

IO-$TiO_2$/NRs, and IO-$TiO_2$/NRs-$TiO_2$ exhibit strong UV absorption (Fig. S12†). Notably, IO-$TiO_2$/NRs-$TiO_2$ demonstrates the highest visible light absorption among them due to two key factors: (1) the inverse opal structure enhances light absorption through multiple scattering events. (2) The presence of multi-heterojunctions (phase and facet heterojunctions) facilitates efficient charge separation and leads to a redshift in the absorption edge.[32]

To elucidate the role of a multi-heterojunction structure in the IO-$TiO_2$/NRs-$TiO_2$ photoanode, we prepared three comparative samples (IO-$TiO_2$/$TiO_2$, FTO-NRs, and NRs-$TiO_2$) as reference materials. The scanning electron microscopy (SEM) image reveals the presence of numerous $TiO_2$ nanosheets on the surface of IO-$TiO_2$ (Fig. S13a†), while distinct nanostructures are observed for FTO-$TiO_2$ and NRs-$TiO_2$ (Fig. S13b and c†). Additionally, both IO-$TiO_2$/$TiO_2$ and NRs-$TiO_2$ exhibit positive shifts in their Ti 2p peaks compared to FTO-NRs (Fig. S14a†), with a similar shift observed for the binding energy of hydroxyl oxygen in IO-$TiO_2$/$TiO_2$, FTO-NRs and NRs-$TiO_2$ (Fig. S14b†). These findings confirm the successful synthesis of IO-$TiO_2$/$TiO_2$, FTO-NRs and NRs-$TiO_2$ catalysts. The linear sweep voltammetry (LSV) measurements were conducted on various photoanodes prepared using the as-synthesized catalysts under sunlight illumination. All samples exhibited negligible current densities in the absence of light (Fig. 4a). Under light irradiation, IO-$TiO_2$, IO-$TiO_2$/$TiO_2$, and FTO-NRs exhibited photocurrent densities of 0.14, 0.23, and 0.35 mA $cm^{-2}$ at 1.23 V *vs.* RHE, respectively (Fig. S15†). After constructing a facet heterojunction and phase heterojunction, the photocurrent density increases to 0.43 and 0.71 mA $cm^{-2}$, respectively, at the same potential. These results demonstrate that both types of heterojunctions significantly enhance the PEC performance. More importantly, IO-$TiO_2$/NRs-$TiO_2$ notably exhibits the highest photocurrent density (1.01 mA $cm^{-2}$), which is 2.3 and 1.4 times higher than that of NRs-$TiO_2$ and IO-$TiO_2$/NRs, respectively, demonstrating comparable values to those reported by other research groups (Table S1†). In addition, compared to the original IO-$TiO_2$, the onset potential of IO-$TiO_2$/NRs and IO-$TiO_2$/NRs-$TiO_2$ exhibited a cathodic shift of approximately 334 mV, with a steeper curve slope observed after the peak. This suggests that the heterojunction-modified catalyst possesses higher catalytic activity and faster kinetics. Although the photocurrent of IO-$TiO_2$/NRs increases more rapidly in the range of 0.2 to 0.5 V *vs.* RHE, it tends to saturate as the potential continues to increase. In contrast, the photocurrent of IO-$TiO_2$/NRs-$TiO_2$ continues to increase rapidly up to 0.8 V *vs.* RHE, indicating superior catalytic kinetics. These results indicate the enhanced light-harvesting efficiency attributed to the presence of multiple heterojunctions.

The efficiency of a photoanode in producing hydrogen from solar energy in a semi-electrolytic cell can be quantified using the applied bias photon-to-current efficiency (ABPE). As illustrated in Fig. S16a,† IO-$TiO_2$/NRs-$TiO_2$ exhibits a peak ABPE value of 0.387% at 0.68 V *vs.* RHE, which is higher than that of IO-$TiO_2$ (0.351%) and bare $TiO_2$ (0.026%). This observed enhancement in ABPE confirms that rutile $TiO_2$ facilitates charge transfer by accepting holes, thereby significantly improving the water splitting efficiency of the photoanode. Furthermore, compared to IO-$TiO_2$ and bare $TiO_2$, IO-$TiO_2$/NRs-$TiO_2$ demonstrates superior charge separation efficiency at 1.23 V *vs.* RHE, indicating that multi-heterojunction $TiO_2$ can effectively achieve spatial separation of photogenerated carriers (Fig. S16b†). The incident photon to current conversion efficiency (IPCE) of the photoanode was measured at 1.23 V *vs.* RHE

using a single wavelength filter, power meter, and light source. Fig. 4b illustrates that IO-$TiO_2$ exhibits the lowest IPCE. However, upon introducing a heterojunction, an enhanced IPCE is achieved in the wavelength range of 400–430 nm for IO-$TiO_2$/NRs (anatase/rutile-phase heterojunction), while IO-$TiO_2$/NRs-$TiO_2$ demonstrates the maximum IPCE value due to its multi-heterojunction structure which facilitates efficient charge separation and transfer.[33] Furthermore, as shown in Fig. 4c, IO-$TiO_2$/NRs-$TiO_2$ demonstrates excellent photostability, and maintains 94.6% of the initial photocurrent at 1.23 V *vs.* RHE for 5 h. Moreover, no significant changes in the morphology and the crystal structure of the IO-$TiO_2$/NRs-$TiO_2$ photoanode were found after long-term stability tests, characterized by SEM (Fig. S17a†) and XRD (Fig. S17b†). The hydrogen evolution measurements were conducted to assess the water splitting activity of IO-$TiO_2$, IO-$TiO_2$/NRs, and IO-$TiO_2$/NRs-$TiO_2$. As displayed in Fig. 4d, under the influence of 10% triethanolamine (v/v) as a sacrificial reagent, the kinetics of $H_2$ production exhibits an almost linear increase with irradiation time. IO-$TiO_2$ demonstrates a relatively low rate of $H_2$ production due to its high recombination rate of photoinduced charge pairs. Conversely, IO-$TiO_2$/NRs displays an enhanced rate of $H_2$ production attributed to the presence of an anatase/rutile-phase heterojunction facilitating charge separation. Notably, among all tested photoanodes, IO-$TiO_2$/NRs-$TiO_2$ showcases superior performance in terms of hydrogen production with a yield reaching approximately 2046 μmol $g^{-1}$ after 3 h, which is about 1.6 and 3 times higher than that achieved by IO-$TiO_2$/NRs and IO-$TiO_2$, respectively. Notably, IO-$TiO_2$/NRs-$TiO_2$ without any metal doping exhibits a hydrogen production rate comparable to that of other studies on rutile or anatase $TiO_2$ with Pt loading (Table S2†), indicating that the construction of multiple heterojunctions promotes efficient separation of photogenerated charges.[10] Furthermore, no significant decrease in activity is observed for IO-$TiO_2$/NRs-$TiO_2$ after 9 times of continuous testing, suggesting that the 3D multi-heterojunction structure remains highly stable for $H_2$ evolution.

To demonstrate the capability of a multi-heterojunction in facilitating charge-carrier separation, a series of photoluminescence (PL) measurements were conducted. In comparison to IO-$TiO_2$, a noticeable reduction in emission intensity is observed for IO-$TiO_2$/NRs (Fig. 5a), indicating that the anatase/rutile-phase heterojunction effectively mitigates recombination of photogenerated electron–hole pairs. Importantly, the significant decrease in emission intensity for IO-$TiO_2$/NRs-$TiO_2$ compared to IO-$TiO_2$/NRs highlights efficient charge separation facilitated by multiple heterojunctions, promoting electron separation and conduction band shifting, thereby enhancing luminescence annihilation. Furthermore, time-resolved photoluminescence (TRPL) measurements were employed to investigate the lifetimes of electron–hole pairs. The average lifetimes ($\tau_{ave}$) for IO-$TiO_2$, IO-$TiO_2$/NRs, and IO-$TiO_2$/NRs-$TiO_2$ are approximately 1.26 ns, 1.83 ns, and 5.13 ns respectively (Fig. 5b and Table S3†). Notably, the $\tau_{ave}$ of charge carriers in IO-$TiO_2$/NRs-$TiO_2$ exhibits a remarkable increase by a factor of 4.07 compared to that in IO-$TiO_2$ and a significant enhancement by a factor of 2.80 compared to that in IO-$TiO_2$/NRs.

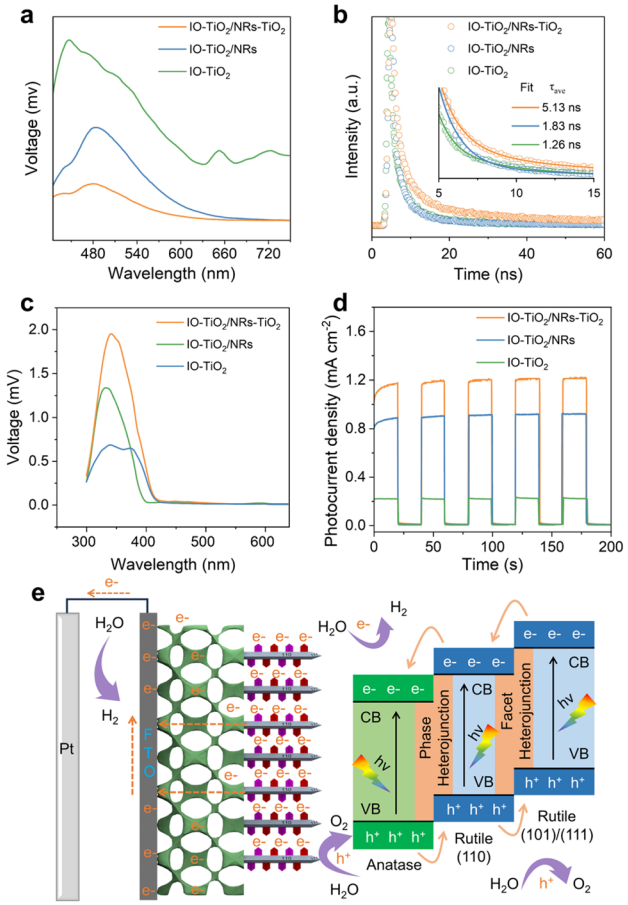


Fig. 5 (a) PL spectra, (b) TRPL spectra, (c) SPV spectra, and (d) photocurrent response of IO-$TiO_2$, IO-$TiO_2$/NRs and IO-$TiO_2$/NRs-$TiO_2$. (e) Schematic diagram of the band alignment and charge transfer in an IO-$TiO_2$/NRs-$TiO_2$ heterojunction, and the light scattering and electron transport in the IO-$TiO_2$/NRs-$TiO_2$ photoanode for water splitting.

Transient-state surface photovoltage (TS-SPV) measurements were further used to investigate the dynamic properties of photoexcited charge separation.[34] As shown in Fig. 5c, IO-$TiO_2$/NRs-$TiO_2$ exhibits the most pronounced response peak compared to IO-$TiO_2$ and IO-$TiO_2$/NRs, once again confirming the efficient separation of photogenerated charges. Moreover, Fig. 5d presents that the photocurrent stabilized at approximately 1.1 mA $cm^{-2}$ upon light illumination, indicating the rapid transfer of photogenerated electrons from NRs/$TiO_2$ to IO-$TiO_2$. Furthermore, when the light is turned off, the photocurrent decays rapidly to a negligible dark current, indicating the rapid transport of photogenerated electrons from the IO-$TiO_2$ backbone to the FTO substrate. In addition, the EIS fitting results reveal that the charge transfer resistances of IO-$TiO_2$, IO-$TiO_2$/NRs, and IO-$TiO_2$/NRs-$TiO_2$ are 342.6 Ω, 111.5 Ω, and 62.2 Ω, respectively (Fig. S18†). These findings indicate that both crystal phase heterojunctions and facet heterojunctions significantly enhance charge transfer efficiency. All these results confirm that a multi-heterojunction can indeed improve the interfacial charge transfer and reduce interfacial reaction resistance, thus greatly

promoting the charge spatial separation and prolonging the lifetime of the excited electrons.[35]

Based on the simulation and experimental results, we propose a mechanistic explanation for the augmented efficiency of charge separation and transfer through the construction of multiple heterojunctions (Fig. 5e). Under light illumination, IO-$TiO_2$/NRs-$TiO_2$ can significantly enhance light collection through multiple scattering between radially oriented nanorods, the coated rutile $TiO_2$ nanosheets and inverse opal, effectively absorbing photons and generating lots of electron–hole pairs. At the $TiO_2$/electrolyte interface, band bending occurs due to the initial difference in electrochemical potential, which drives holes in $TiO_2$ to move into the $TiO_2$/electrolyte interface, thereby oxidizing water to $O_2$. Meanwhile, the photogenerated electrons generated in the rutile crystal face of the coated $TiO_2$ nanosheets are transferred to IO-$TiO_2$ along the NRs, which are then collected by the FTO substrate and subsequently transported to the Pt cathode, reducing water to $H_2$.[10] Notably, the formation of a type II facet heterojunction of NRs-$TiO_2$ can promote the charge separation process in rutile $TiO_2$. And the conduction band of IO-$TiO_2$ is slightly lower, and the band alignment between rutile $TiO_2$ and anatase $TiO_2$ is favourable for electron transfer from rutile to anatase through a phase heterojunction. Therefore, the presence of an anatase/rutile-phase heterojunction and rutile facet heterojunction in the IO-$TiO_2$/NRs-$TiO_2$ samples would greatly facilitate the charge separation and transfer process, thereby enhancing the PEC performance.

## Conclusions

In summary, the strategy of combining a crystal phase heterojunction with a crystal faceted heterojunction is proposed for the first time to enhance $TiO_2$ charge transfer efficiency as well as PEC activity. Specifically, the IO-$TiO_2$/NRs-$TiO_2$ photoanode with a 3D hierarchical structure has been prepared by hydrothermal and calcination methods. Firstly, IO-$TiO_2$ with a periodic void structure favors light absorption. Secondly, the disordered lattice at the anatase/rutile phase junction improves the PEC activity. In addition, the crystal heterojunction of rutile prolongs the photoelectron lifetime through the discontinuous band gap and accelerates the space charge separation. Impressively, the IO-$TiO_2$/NRs-$TiO_2$ photoanode exhibits a current density of 1.12 mA $cm^{-2}$ at 1.23 V *vs.* RHE and a hydrogen production efficiency of 682 μmol $h^{-1}$ $g^{-1}$ under simulated light conditions, which is far superior to that of IO-$TiO_2$ and the single heterojunction of IO-$TiO_2$/NRs. This work provides a new idea for constructing photoanodes with excellent electron–hole separation performance.

## Data availability

All data can be found in the main article or the ESI.†

## Author contributions

S. C. and Z. L. designed the research; C. H., J. C., and Y. X. conducted the research; B. X., C. H., J. C., and Y. X. analyzed the data; B. X., C. H., S. C., and Z. L. wrote the paper.

## Conflicts of interest

There are no conflicts to declare.

## Acknowledgements

This work was financially supported by the National Natural Science Foundation of China (No. U24A20541 and 22278094), Guangdong Graduate Education Innovation Program (No. 2023JGXM_102), Jiangxi Province "Double Thousand Plan" (No. jxsq2023102142), and Basic and Applied Basic Research Program of Guangzhou (No. SL2024A03J00499).

## Notes and references

1 C. Jin, M. Han, Y. Wu and S. Wang, Solar-driven photoelectrochemical conversion of biomass: recent progress, mechanistic insights and potential scalability, *Energy Environ. Sci.*, 2024, **17**, 7459.
2 L. Ran, S. Qiu, P. Zhai, Z. Li, J. Gao, X. Zhang, B. Zhang, C. Wang, L. Sun and J. Hou, Conformal Macroporous Inverse Opal Oxynitride-Based Photoanode for Robust Photoelectrochemical Water Splitting, *J. Am. Chem. Soc.*, 2021, **143**, 7402.
3 Y. Huang, M. Shen, H. Yan, Y. He, J. Xu, F. Zhu, X. Yang, Y.-X. Ye and G. Ouyang, Achieving a solar-to-chemical efficiency of 3.6% in ambient conditions by inhibiting interlayer charges transport, *Nat. Commun.*, 2024, **15**, 5406.
4 B. Li, M. Lv, Y. Zhang, X. Gong, Z. Lou, Z. Wang, Y. Liu, P. Wang, H. Cheng, Y. Dai, B. Huang and Z. Zheng, Single-Particle Imaging Photoinduced Charge Transfer of Ferroelectric Polarized Heterostructures for Photocatalysis, *ACS Nano*, 2024, **18**, 25522.
5 X. Li, W. Zhang, F. Yang, S. Yao, L. Li, X. An, B. Xi, S. Xiong and C. An, Reinforced Electrons Transfer and Capture in S-Scheme $TiO_2$@Co(OH)F-Pt Heterojunction for Excellent Solar Hydrogen Evolution, *Adv. Energy Mater.*, 2024, **14**, 2401877.
6 Y. Gao, M. Zhang, Q. Zhao, W. Liu, L. Zheng, J. Ouyang and N. Na, Regulating the electron spin orbital by sulfur doping of Ti vacancies to manipulate spin flip for enhancing PEC water splitting performance, *Energy Environ. Sci.*, 2024, **17**, 6268.
7 A. C. Wardhana, A. Yamaguchi, K. Adachi, D. Hashizume and M. Miyauchi, Direct Interfacial Excitation from $TiO_2$ to Cu(II) Nanoclusters Enables Cathodic Photoresponse for Hydrogen Evolution under Visible-Light Irradiation, *Small*, 2023, **19**, 2206893.
8 K. Vibulyaseak, A. Kudo and M. Ogawa, Template Synthesis of Well-Defined Rutile Nanoparticles by Solid-State Reaction at Room Temperature, *Inorg. Chem.*, 2020, **59**, 7934.
9 Q. Zhang, X. Liu, C. Du, M. Jin, L. Yang, R. Jiang, X. Ma, Y. Zhu, C. Cao and M. Zou, Fe-doping accelerated magnesium storage kinetics in rutile $TiO_2$ cathode materials, *Chem. Eng. J.*, 2024, **498**, 155812.
10 C. Gao, T. Wei, Y. Zhang, X. Song, Y. Huan, H. Liu, M. Zhao, J. Yu and X. Chen, A Photoresponsive Rutile $TiO_2$

Heterojunction with Enhanced Electron-Hole Separation for High-Performance Hydrogen Evolution, *Adv. Mater.*, 2019, **31**, 1806596.

11 X. Wang, S. Ma, B. Liu, S. Wang and W. Huang, Imperfect makes perfect: defect engineering of photoelectrodes towards efficient photoelectrochemical water splitting, *Chem. Commun.*, 2023, **59**, 10044.

12 Z. Wang, T. D. Nguyen, L. P. Yeo, C. K. Tan, L. Gan and A. I. Y. Tok, Periodic FTO IOs/CdS NRs/CdSe Clusters with Superior Light Scattering Ability for Improved Photoelectrochemical Performance, *Small*, 2020, **16**, 1905826.

13 Q. Pan, A. Li, Y. Zhang, Y. Yang and C. Cheng, Rational Design of 3D Hierarchical Ternary $SnO_2/TiO_2/BiVO_4$ Arrays Photoanode toward Efficient Photoelectrochemical Performance, *Adv. Sci.*, 2020, **7**, 1902235.

14 Z. Wang, X. Li, H. Ling, C. K. Tan, L. P. Yeo, A. C. Grimsdale and A. I. Y. Tok, 3D FTO/FTO-Nanocrystal/$TiO_2$ Composite Inverse Opal Photoanode for Efficient Photoelectrochemical Water Splitting, *Small*, 2018, **14**, 1800395.

15 Q. Pan, H. Zhang, Y. Yang and C. Cheng, 3D Brochosomes-Like $TiO_2/WO_3/BiVO_4$ Arrays as Photoanode for Photoelectrochemical Hydrogen Production, *Small*, 2019, **15**, 1900924.

16 F. Ma, X. Xu, C. Huo, C. Sun, Q. Li, Z. Yin and S. Cao, Dual Heterogeneous Structures Promote Electrochemical Properties and Photocatalytic Hydrogen Evolution for Inverse Opal ZnO/ZnS/$Co_3O_4$ Crystals, *Inorg. Chem.*, 2024, **63**, 8782.

17 D. Padayachee, A. S. Mahomed, S. Singh and H. B. Friedrich, Effect of the $TiO_2$ Anatase/Rutile Ratio and Interface for the Oxidative Activation of *n*-Octane, *ACS Catal.*, 2020, **10**, 2211.

18 X. Li, S. Anwer, Q. Guan, D. H. Anjum, G. Palmisano and L. Zheng, Coupling Long-Range Facet Junction and Interfacial Heterojunction *via* Edge-Selective Deposition for High-Performance Z-Scheme Photocatalyst, *Adv. Sci.*, 2022, **9**, 2200346.

19 Y. He, J. Zhu, Y. Yuan, M. Li, Y. Yang, Y. Liu, M. Chen, D. Cao and X. Yan, Dual-regulation charge separation strategy with the synergistic effect of 1D/0D heterostructure and inserted ferroelectric layer for boosting photoelectrochemical water oxidation, *J. Mater. Chem. A*, 2021, **9**, 7594.

20 X. Lv, D. Pan, S. Zheng, M. Zeeshan Shahid, G. Jiang, J. Wang and Z. Li, *In situ* producing $CsPbBr_3$ nanocrystals on (001)-faceted $TiO_2$ nanosheets as S-scheme heterostructure for bifunctional photocatalysis, *J. Colloid Interface Sci.*, 2023, **652**, 673.

21 X. Ke, P. Wang, X. Wang, F. Chen and H. Yu, Directionally charging d-orbital electron of $Mo_2C$ MXene *via in situ* coupled $MoSe_2$ nanosheets for exceptional photocatalytic $H_2$ generation, *Chem. Eng. J.*, 2024, **495**, 153477.

22 X. Wang, Z. Wang, Y. Li, J. Wang and G. Zhang, Efficient photocatalytic $CO_2$ conversion over 2D/2D Ni-doped $CsPbBr_3/Bi_3O_4Br$ Z-scheme heterojunction: critical role of Ni doping, boosted charge separation and mechanism study, *Appl. Catal., B*, 2022, **319**, 121895.

23 F. Xu, K. Meng, B. Cheng, S. Wang, J. Xu and J. Yu, Unique S-scheme heterojunctions in self-assembled $TiO_2/CsPbBr_3$ hybrids for $CO_2$ photoreduction, *Nat. Commun.*, 2020, **11**, 4613.

24 X.-T. Li, L. Chen, C. Shang and Z.-P. Liu, *In Situ* Surface Structures of PdAg Catalyst and Their Influence on Acetylene Semihydrogenation Revealed by Machine Learning and Experiment, *J. Am. Chem. Soc.*, 2021, **143**, 6281.

25 J. Yu, A. L. Godiksen, A. Mamahkel, F. Søndergaard-Pedersen, T. Rios-Carvajal, M. Marks, N. Lock, S. B. Rasmussen and B. B. Iversen, Selective Catalytic Reduction of NO Using Phase-Pure Anatase, Rutile, and Brookite $TiO_2$ Nanocrystals, *Inorg. Chem.*, 2020, **59**, 15324.

26 S. Wang, J. Yao, Z. Ou, X. Wang, Y. Long, J. Zhang, Z. Fang, T. Wang, T. Ding and H. Xu, Plasmon-assisted nanophase engineering of titanium dioxide for improved performances in single-particle based sensing and photocatalysis, *Nanoscale*, 2022, **14**, 4705.

27 Z. Yin, X. Zhang, X. Yuan, W. Wei, Y. Xiao and S. Cao, Constructing $TiO_2@Bi_2O_3$ multi-heterojunction hollow structure for enhanced visible-light photocatalytic performance, *J. Cleaner Prod.*, 2022, **375**, 134112.

28 T. Zhang, P. Zheng, J. Gao, X. Liu, Y. Ji, J. Tian, Y. Zou, Z. Sun, Q. Hu, G. Chen, W. Chen, X. Liu, Z. Zhong, G. Xu, T. Zhu and F. Su, Simultaneously activating molecular oxygen and surface lattice oxygen on Pt/$TiO_2$ for low-temperature CO oxidation, *Nat. Commun.*, 2024, **15**, 6827.

29 C. Yang, W. Ling, Y. Zhu, Y. Yang, S. Dong, C. Wu, Z. Wang, S. Yang, J. Li, G. Wang, Y. Huang, B. Yang, Q. Cheng, Z. Liu and H. Yang, Surface hydroxylation engineering to boost oxygen evolution reaction on $IrO_2/TiO_2$ for PEM water electrolyzer, *Appl. Catal., B*, 2024, **358**, 124462.

30 P. Zhang, Y. Li, Y. Zhang, R. Hou, X. Zhang, C. Xue, S. Wang, B. Zhu, N. Li and G. Shao, Photogenerated Electron Transfer Process in Heterojunctions: *In Situ* Irradiation XPS, *Small Methods*, 2020, **4**, 2000214.

31 B. Sun, C. Huang, C. Yang, D. Ke, Y. Liu, Q. Lu, X. Liu, X. Xiong, Y. Chen, Q. Jiang, J. Hu and T. Zhou, Atomic interfacial charge and energy transfer paths at $MoS_2$/Pd bonded defect-rich BiOCl interfaces for efficient photocatalysis, *Appl. Catal., B*, 2024, **345**, 123720.

32 X. Huang, W. Gu, S. Hu, Y. Hu, L. Zhou, J. Lei, L. Wang, Y. Liu and J. Zhang, Phosphorus-doped inverse opal g-$C_3N_4$ for efficient and selective CO generation from photocatalytic reduction of $CO_2$, *Catal. Sci. Technol.*, 2020, **10**, 3694.

33 S. Lin, H. Ren, Z. Wu, L. Sun, X.-G. Zhang, Y.-M. Lin, K. H. L. Zhang, C.-J. Lin, Z.-Q. Tian and J.-F. Li, Direct Z-scheme $WO^{3-}$ nanowire-bridged $TiO_2$ nanorod arrays for highly efficient photoelectrochemical overall water splitting, *J. Energy Chem.*, 2021, **59**, 721.

34 N. Yuan, J. Zhang, S. Zhang, G. Chen, S. Meng, Y. Fan, X. Zheng and S. Chen, What Is the Transfer Mechanism of Photoexcited Charge Carriers for g-$C_3N_4/TiO_2$ Heterojunction Photocatalysts? Verification of the Relative p–n Junction Theory, *J. Phys. Chem. C*, 2020, **124**, 8561.

35 M. Bhatt, P. K. Nayak and D. Ghosh, Data-Driven Design of Electroactive Spacer Molecules to Tune Charge Carrier Dynamics in Layered Halide Perovskite Heterostructures, *ACS Nano*, 2024, **18**, 24484.